

# Frequency-Domain Modeling of Orbit and Clock Errors for Sequential Positioning

Elisa Gallon, *Illinois Institute of Technology*  
Mathieu Joerger, *Virginia Tech*  
Boris Pervan, *Illinois Institute of Technology*

## BIOGRAPHIES

**Elisa Gallon** received her Bachelor's Degree in Mathematics from Université Blaise Pascal, France in 2014 and her Master of Science in Global Navigation Satellite Systems from ENAC and ISAE-Supaéro in 2016. From 2016 to 2017, she worked at the European Space Agency (ESA) on Orbit Determination and Time Synchronization of Galileo satellites. She is currently a Ph.D. Candidate at the Navigation Laboratory in the Department of Mechanical and Aerospace Engineering at Illinois Institute of Technology (IIT) in Chicago.

**Dr. Mathieu Joerger** obtained a Master in Mechatronics from the National Institute of Applied Sciences in Strasbourg, France, in 2002. He earned a M.S. in 2002 and a Ph.D. in 2009 in Mechanical and Aerospace Engineering at IIT in Chicago. He is the 2009 recipient of the Institute of Navigation (ION) Bradford Parkinson award, and the 2014 recipient of the (ION) Early Achievement Award. He is also an Associate Editor of Navigation for the Institute of Electrical and Electronics Engineers (IEEE) Transactions on Aerospace and Electronic Systems. Dr. Joerger is currently assistant professor at Virginia Tech, in Blacksburg, VA, working on multi-sensor integration for safe navigation and collision warning of automated driving systems (ADS). He is a member of the E.U./U.S. Advanced RAIM (ARAIM) Working Group C.

**Dr. Boris Pervan** is a Professor of Mechanical and Aerospace Engineering at IIT, where he conducts research on advanced navigation systems. Prior to joining the faculty at IIT, he was a spacecraft mission analyst at Hughes Aircraft Company (now Boeing) and a postdoctoral research associate at Stanford University. Prof. Pervan received his B.S. from the University of Notre Dame, M.S. from the California Institute of Technology, and Ph.D. from Stanford University. He is an Associate Fellow of the AIAA, a Fellow of the Institute of Navigation (ION), and Editor-in-Chief of the ION journal NAVIGATION. He was the recipient of the IIT Sigma Xi Excellence in University Research Award (2011, 2002), Ralph Barnett Mechanical and Aerospace Dept. Outstanding Teaching Award (2009, 2002), Mechanical and Aerospace Dept. Excellence in Research Award (2007), University Excellence in Teaching Award (2005), IEEE Aerospace and Electronic Systems Society M. Barry Carlton Award (1999), RTCA William E. Jackson Award (1996), Guggenheim Fellowship (Caltech 1987), and Albert J. Zahm Prize in Aeronautics (Notre Dame 1986).

## ABSTRACT

In this paper, we develop new stochastic orbit and clock error models for positioning, fault detection, and integrity monitoring over time. This work is intended for time-sequential navigation systems including Global Navigation Satellite Systems (GNSS) integrated with inertial navigation systems (INS) or dual-frequency, multi-constellation, sequential Advanced Receiver Autonomous Integrity Monitoring (ARAIM).

## INTRODUCTION

GNSS provides worldwide positioning but requires the visibility of four or more satellites and is vulnerable to jamming and spoofing attacks. On the other hand, INS can be used as a dead reckoning sensor to estimate displacements over time with respect to an initial position. INS-based estimation errors drift due to the integration of sensor errors over time. Combining INS and GNSS, for example in a Kalman Filter (KF), can limit the drift in INS positioning errors while providing continuity through sky-obstructed areas and robustness against external GNSS jamming and spoofing attacks [1]. GNSS/INS integration relies on filtering measurements over time, which, in turn, requires robust modeling of stochastic errors, including time correlation.

For aircraft navigation, the baseline version of ARAIM uses carrier smoothed code (CSC) measurements at one instant in time to provide a ‘snapshot’ navigation solution [2], [3], [4]. However, in [5], we showed that the additional exploitation of satellite motion over time provides superior positioning performance and tighter PLs than baseline ARAIM. Sequential ARAIM algorithms (KF, for example) open the possibility to extend the scope of ARAIM applications beyond aircraft navigation, to rail, harbor, or arctic operations.

To implement time-sequential ARAIM or inertial-GNSS integration, one must ensure that the error models implemented in the KF properly account for time correlation. In both applications, dynamic models for three main GNSS error sources are needed: orbit and clock errors, tropospheric delay, and multipath. It was shown in [6] and [7] that assuming a large measurement error correlation time constant does not necessarily guarantee an upper bound on the positioning error variance. More sophisticated methods are needed, such as those also developed in [6] and [7]. In this paper, following on preliminary work in [8], we now focus on developing robust stochastic models for GNSS orbit and clock errors, which are the main contributors to ranging error for dual-frequency GNSS users.

In [9], over-bounding theory (see also [10], [11]) was used to find upper bounds on the variance of orbit and clock errors for both the GPS and Galileo satellites. Unfortunately, these snapshot models are insufficient for time-sequential implementations because they do not address the stochastic dynamics of these errors over time.

In [6], an analytical bound on the integrity risk for time-sequential linear estimators was developed using Autocorrelation Function (ACF) bounding. This approach, although simple to implement, requires continuous, cumulative storage of all data used by the estimator, and therefore is not suitable for KF implementations, except for low-order systems and very short time intervals. More recently, the concept of Power Spectral Density (PSD) bounding, which was used in [12], has proven to be much more flexible and powerful than ACF bounding. [13] outlines an integrity monitoring method using Power Spectral Density (PSD) bounding. It also has the advantages of being less restrictive and more intuitive than autocorrelation bounding. Modeling by PSD bounding is compatible with Kalman filtering, and is not restricted to fixed-interval implementations, unlike ACF bounding.

In this work, we derive new GNSS orbit and clock error models using PSD bounding. Clock errors are analyzed per satellite clock type (Rubidium versus Cesium for GPS, and Rubidium versus Passive Hydrogen Masers for Galileo), considering both the orbit and clock error distributions, and their PSDs.

## **ORBIT AND CLOCKS ERROR CHARACTERIZATION OVER TIME**

This section describes the process used to generate orbit and clock errors. Input repositories are described as well as the data they contain. To generate orbit and clock errors, two types of inputs are required: reference and broadcast navigation data. Both of these data files are obtained from the Multi-GNSS EXperiment (MGEX) repositories. The following two sub-sections describe these inputs.

### **Reference orbit and clocks**

The MGEX service was initiated by the International GNSS Service (IGS) to create a single GNSS data service for multiple constellations. MGEX is comprised of several Analysis Centers (ACs) which independently compute their own GNSS orbit and clock products. For this work, we use precise orbit data from two ACs: CODE for GPS and CNES for Galileo, and we will consider them to be our truth reference (see repository [14]). Note that the reference products have an accuracy of 2.5 cm (orbit accuracies are 1D mean RMS values over the three XYZ geocentric components). Because we are interested in characterizing orbit and clock errors over relatively short periods of time (several hours), the 15 min sampling period of these files is insufficient, so the data is therefore interpolated to 30 s. In this paper we use an 8<sup>th</sup> order Lagrange polynomial (according to the analysis in [15]). Clocks errors are random walk processes and should not be interpolated. Instead, we use the clock products directly from IGS, which are provided at a 30 s sampling interval.

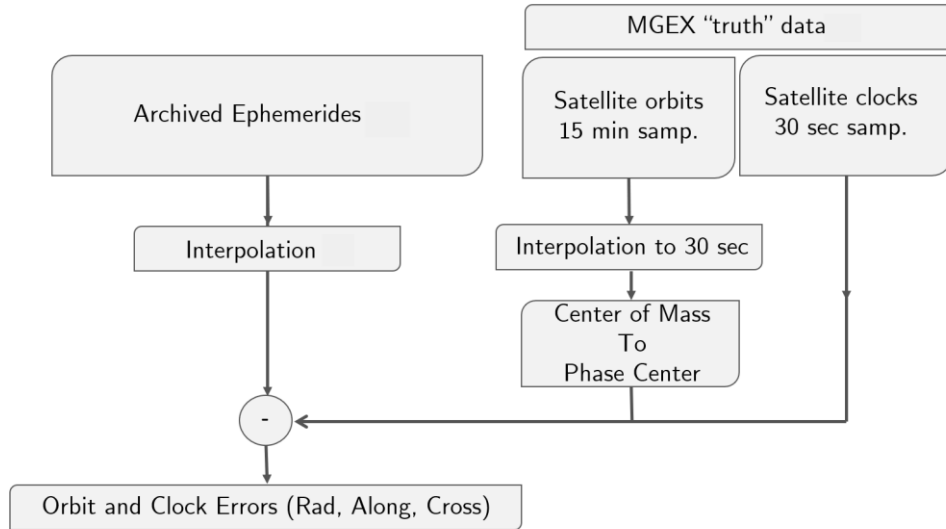


Figure 1: Errors generation

### Broadcast ephemerides

Broadcast ephemerides are stored in Receiver Independent Exchange (RINEX) formats that contain 24 hours of navigation message. This work makes use of Stanford University's 'sugl' files for GPS satellites and 'brdc' from CNES for Galileo (see repositories [16] and [17]). Those institutions were chosen among several others because their cleaning and validation algorithms ensured a limited amount of residual file recording, storing, and labeling errors.

### Orbit and clock errors

Satellite orbit and clock errors are obtained by differencing the satellite orbit and clock derived from the broadcast ephemerides from the reference orbits (as shown in Figure 1). Reference orbits are provided with respect to the center of mass (CoM) of the satellite, whereas broadcast ephemerides are decoded with respect to the satellite's antenna phase center (APC), hence they need to be converted to the same reference point (in this case, the APC). The offset for this conversion is provided in the ANTenna EXchange (ANTEX) files [18] for each GPS and Galileo satellites. After correcting for the offset, orbit and clock errors are obtained by differencing reference and broadcast orbit and clocks. The final errors are then converted to the satellite-referenced radial, along-track, and cross-track frame. Note that ranging errors are affected by two types of errors: the clock errors which are non-dimensional and affect every direction equally, and the projection of the satellite position error onto the line of sight, which is mainly radial. Therefore, orbit and clock errors are computed as radial-plus-clock errors. Figure 2 shows example radial-plus-clock errors for the GPS and Galileo satellites in December 2018.

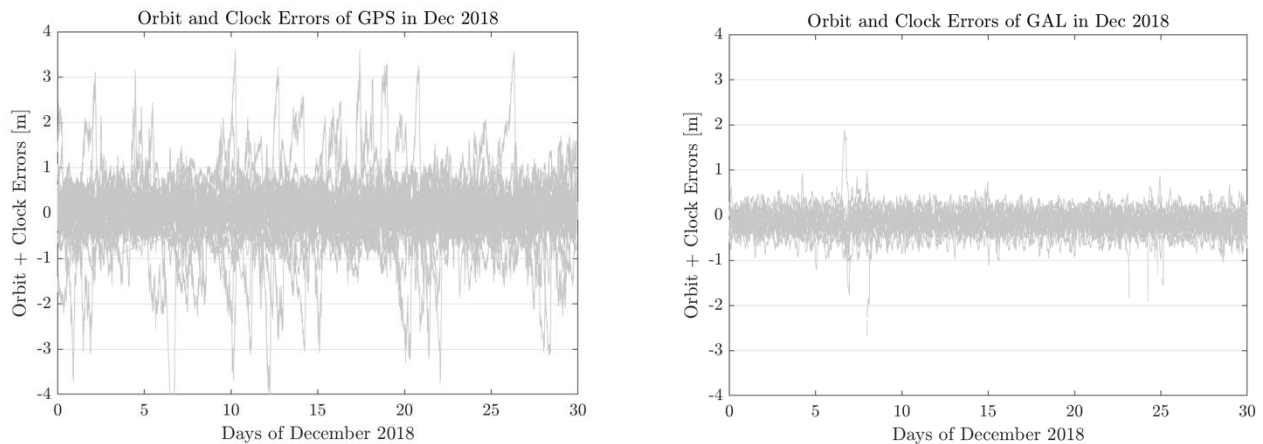


Figure 2: Time evolution of Radial Plus Clock errors for GPS (left) and Galileo (right) satellites in December 2018

In addition, GPS ephemerides are broadcast every 2 hours. When a new set of GPS ephemerides is received, the old one is still valid for two more hours, although most users will decide to use the new set as soon as they receive it. This new upload creates a ‘jump’ in the estimated satellite position. To mitigate this effect, the broadcast ephemerides from the current and following sets of ephemerides are interpolated in the position domain to ensure a continuous transition over the two-hour overlap period. The process used for Galileo ephemerides is similar and is explained in [8].

### Impact of satellite clock on orbit and clock errors

There exist three main categories of space-qualified atomic clocks used for satellite navigation: Rubidium or Rubidium Atomic Frequency Standard (Rb or RAFS), Cesium (Cs), and Passive Hydrogen Maser (PHM). Over the years, GPS satellites have been equipped with several combinations of the clocks. GPS blocks II/IIA carried two Cs and two Rb clocks, blocks IIR and IIR-M contained three Rb clocks, and blocks IIF contained two Rb and one Cs clocks. Galileo satellites, on the other hand, use PHM as their primary clocks and RAFS as secondary. Table 1 and Table 2 summarize the GPS and Galileo clocks and block numbers associated with each PRN for the time periods considered in this work (year 2018).

PRN	1	2	3	5	6	7	8	9	10	11	12	13	14	15	16	17
<b>Clock</b>	Rb	Rb	Rb	Rb	Rb	Rb	Cs	Rb	Rb	Rb	Rb	Rb	Rb	Rb	Rb	Rb
<b>Block</b>	IIF	IIR	IIF	IIR	IIF	IIR	IIF	IIF	IIF	IIR	IIR	IIR	IIR	IIR	IIR	IIR

PRN	18	19	20	21	22	23	24	25	26	27	28	29	30	31	32
<b>Clock</b>	Rb	Rb	Rb	Rb	Rb	Rb	Cs	Rb	Rb	Rb	Rb	Rb	Rb	Rb	Rb
<b>Block</b>	IIA	IIR	IIR	IIR	IIR	IIR	IIF	IIF	IIF	IIF	IIR	IIR	IIF	IIR	IIF

Table 1: Clocks and blocks of each GPS satellite as of the period of this study (2018)

From Table 1, we can see that most GPS satellites are using a Rb clock as their main clock. Only two satellites use Cs clocks. From Table 2, we can see that most Galileo satellites are PHM satellites and that only 3 of them are RAFS.

PRN	1	2	3	5	7	8	9	11	12	13	14	15	18
<b>Clock</b>	PHM	PHM	PHM	PHM	PHM	PHM	PHM	RAFS	PHM	PHM	PHM	PHM	PHM

PRN	19	20	21	22	24	25	26	27	30	31	33	36
<b>Clock</b>	PHM	RAFS	PHM	RAFS	PHM	PHM	PHM	PHM	PHM	PHM	PHM	PHM

Table 2: Clocks of each Galileo satellite as of the period of this study (2018)

A comparison in [19] of atomic frequency standards among the various constellation for timescales ranging from 1 s to 1 day showed that the stabilities among various clock types could differ by a factor of up to 10 and were generally better for Rb and PHM clocks (in particular, GPS IIF Rb and Galileo PHM ).

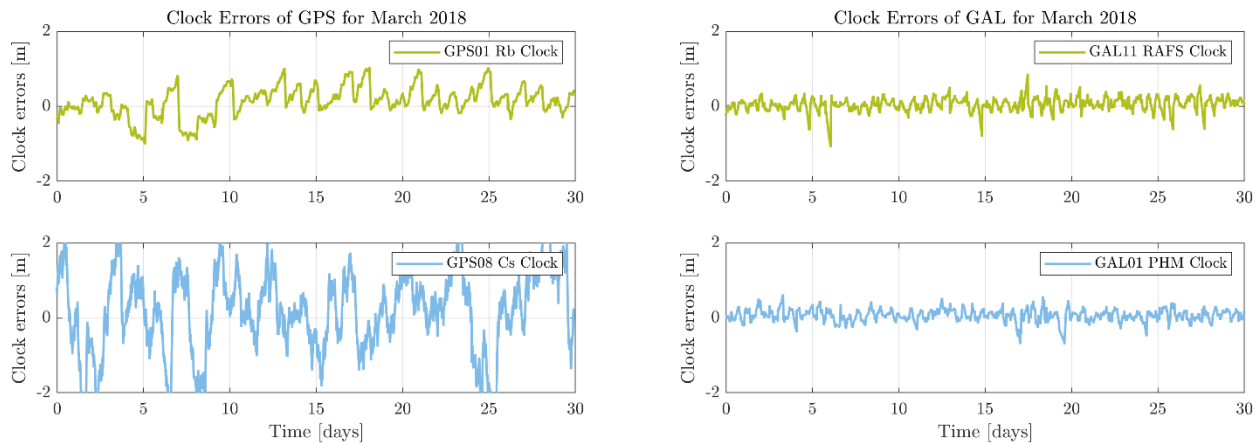


Figure 3: Time series of GPS (left) and GAL (right) orbit and clock errors for various satellite clocks

This observation is illustrated in Figure 3, which shows example time series of GPS (left) and Galileo (right) clock errors for each satellite clock type during March 2018. For GPS, the upper plot shows the clock error of the Rb clock of PRN01 and the lower plot shows the same for the Cs clock of PRN08. The Rb clocks seem to be more stable and oscillate within  $\pm 1$  m. The Cs clock on the other hand has larger error variations that reach up to  $\pm 2$  m. For Galileo clocks however, both PHM and RAFS clock errors have a similar behavior and remain between  $\pm 0.5$  m. The difference between satellite clock errors are therefore more prominent in GPS than in Galileo.

Before attempting to model any observed orbit and clock errors, we must first ensure that they are stationary over the durations used in the modeling.

## ORBIT AND CLOCK ERRORS STATIONARITY ANALYSIS

For any random process  $X$ , let us define the autocorrelation function  $R_{XX}$  of  $X$  as:

$$R_{XX}(\xi) = E[X(t)X(t + \xi)] \quad (1)$$

Reference [9] determined bounds on the variances of orbit and clock errors. However, the purpose of this work is to study the time correlation of the orbit and clock errors. Therefore, we are interested in the ACFs of those errors, and not just their values at zero. When dealing with sample autocorrelation functions, a recurrent dilemma arises between stationarity and autocorrelation estimate accuracy. If we use too little data, the autocorrelation will most likely not be accurate due to the expectation operation in Equation (1), but if we use very long sets of data, the process may not be stationary over the entire period.

Let us assume that the autocorrelation function of radial-plus-clock errors is a first-order Gauss Markov Random Process (GMRP) with the following autocorrelation function:

$$\hat{R}_{XX}(t) = \sigma_X^2 e^{-|t|/\tau} \quad (2)$$

where

- $\tau$  is the time constant of the GMRP
- $\sigma_X^2$  is the variance of the random process  $X$

Using this assumption, in [8] we established an upper bound on the variance of the normalized ACF estimate for a first-order GMRP, depending on the process time constant  $\tau$  and the length of data  $T$  used in the estimation of the ACF:

$$\sigma_{\hat{R}_{XX}}^2 \leq \sigma_X^4 \left( \frac{\tau}{T} + \frac{2t + \tau}{T} e^{-2t/\tau} \right) \quad (3)$$

Figure 4 shows the upper bound on the standard deviation of the ACF estimate from Equation (3) as a function of lag time (x-axis) for various lengths of data  $T$  (the different curves). Note that the standard deviations (y-axis) are expressed in meters squared because these are the units of the ACFs of the orbit and clock errors.

At lag time zero, the plot shows the standard deviation of the sample variance estimate error (i.e., the different curves capture the uncertainty in variance estimation error as a function of the length of data used). Using 14 days of data, the standard deviation of the ACF estimate is close to  $0.13 \text{ m}^2$  at lag of 80 hours, whereas using 1 year of data the standard deviation of about  $0.025 \text{ m}^2$  at the same lag. The results in Figure 4 shows that the longer the data used to estimate the ACF, the lower the uncertainty. Note that in this work, we present two approaches to orbit and clock error bounding. The first one makes use of normalized ACF and the second one uses non-normalized ACF. Note that the conclusions obtained with Figure 4 are also valid if we had studied normalized ACFs instead (see [8]).

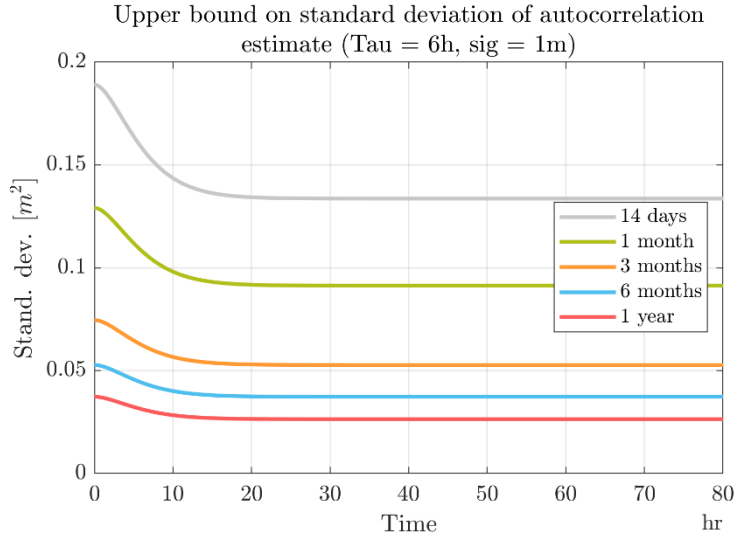


Figure 4: Variance of Autocorrelation Estimate for different length of data

In prior work [8], we began the analysis by determining the maximum length of time over which the experimental error data was stationary. Starting with two weeks of data (half lunar cycles), we looked at orbit and clock ACFs over this duration and observed a dispersion between the various 2-weeks periods. However, this dispersion was smaller or equal to the standard deviations predicted in the 14 days curve mentioned above. This suggested that the data was indeed stationary over this duration. To improve the accuracy of our ACF estimates, we then tried using one month of data. The results obtained were inconclusive and seemed to vary from one month to the other.

In this paper, we will use a more mathematical approach to test for the stationarity of the data. A combination of the Levene test and the two-sample Kolmogorov-Smirnov test was used. The Levene test [20] compares the variances of two or more sets of data. It tests the null hypothesis according to which the variances of the populations are equal (homoscedastic). The two-sample Kolmogorov-Smirnov test [21] determines whether two samples come from the same distribution. Both tests were performed with a 95% confidence level (i.e. p-value of 0.05).

If both tests come back positive (all variances are equal and all data sets come from the same distribution), the data is considered stationary. However, both tests assume that the samples are independent. This is not the case for the actual orbit and clock error data. To approximate the effective number of independent samples we use the properties of a first-order GMRP. Two samples of a first-order GMRP with time constant  $T_c$  can be considered independent if they are separated by a period larger than or equal to  $2 \cdot T_c$ . Therefore, to test stationarity, the data was re-sampled at regular  $2 \cdot T_c$  intervals.

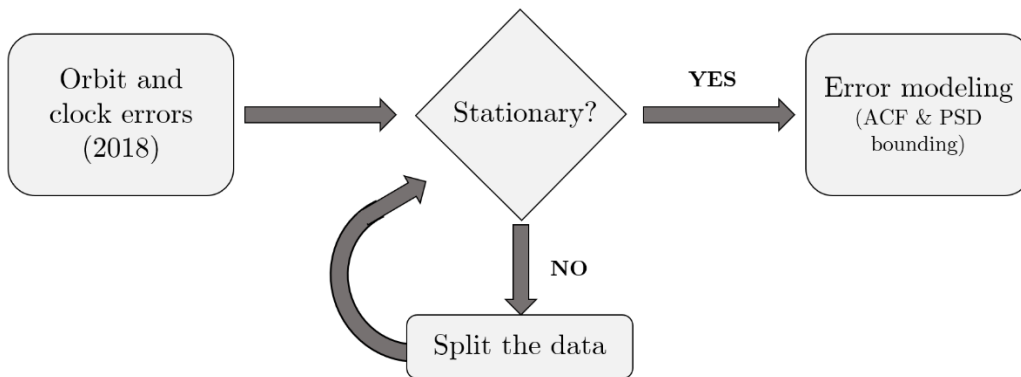


Figure 5: Length of data selection based on stationarity

We use the process described in Figure 5. For each PRN, the orbit and clock errors of a given satellite over 12 months of data are tested first for stationarity. If the dataset is deemed non-stationary, the data is divided into stationary datasets. Once stationarity has been asserted, the orbit and clock errors can be modeled.

## ORBIT AND CLOCK ERROR MODELING OVER TIME

In their prior work, the authors of [9] developed a bound on the variance of orbit and clock errors for GPS and Galileo, based on several years of data. Because the focus was on bounding the variance, and not the entire autocorrelation function, reference [9] does not provide any information on the time correlation of these errors. Therefore, this model was insufficient for applications including time-sequential ARAIM or GNSS/INS integration. Here, we present two possible approaches to modeling these errors over time.

### Zero mean assumption

This section demonstrates that the orbit and clock errors can be assumed zero mean. Figure 6 represents box plots of the error data for each of the PRN of the GPS (upper) and Galileo (lower) constellations. The x-axis represents the satellite's PRN number. The color of the plots indicates the length of data used to generate this boxplot (as determined using the stationarity tests). In a boxplot figure, the middle line represents the sample median and the upper and lower limits of the box represent the 75<sup>th</sup> and 25<sup>th</sup> percentiles, respectively. The vertical lines reaching away from the boxes represent the lowest and highest data points, excluding the outliers, which are represented by colored dots outside of the boxes. A point is considered to be an outlier if it is greater than  $q_3 + 2.7\sigma \times (q_3 - q_1)$  or smaller than  $q_1 - 2.7\sigma \times (q_3 - q_1)$ , where  $q_1$  and  $q_3$  are the 25<sup>th</sup> and 75<sup>th</sup> percentiles of the sample data. Note that  $\pm 2.7\sigma$  corresponds to 99% of the data if it is normally distributed. For both GPS and Galileo, both boxplots seem to rule in favor of a zero-mean assumption: median values of each datasets are close to zero. Note that GPS PRN 8 and 24 (the two Cesium satellites) have much larger standard deviations than the rest of the GPS satellites.

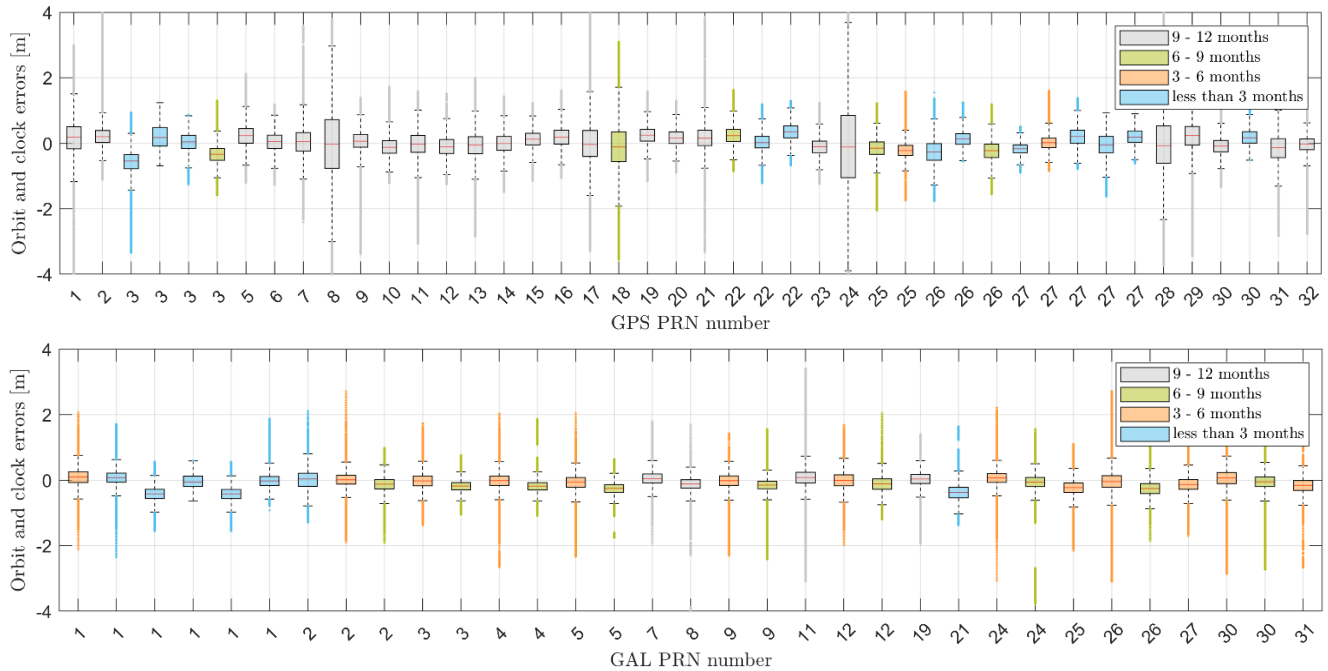


Figure 6: Statistics of the 2018 GPS/GAL Orbit and Clock errors

Given  $\bar{n}$  stationary data sets, let us define the following measurement equation for the estimation of the orbit and clock error means:

$$z = Hx + v \quad (4)$$

where:

- $z$  is an  $\bar{n}$ -by-1 measurement vector of means of stationary data sets  $\bar{x}_i$  for  $i = 1, \dots, \bar{n}$
- $H$  is an  $\bar{n}$ -by-1 observation matrix (in our case a vector of ones)

$x$  is the mean of orbit and clock errors (to estimate)  
 $v$  is the measurement error covariance matrix:

$$V = \begin{bmatrix} \sigma_{\bar{x}_1}^2 & \cdots & 0 \\ \vdots & \ddots & \vdots \\ 0 & \cdots & \sigma_{\bar{x}_n}^2 \end{bmatrix}$$

For each stationary data set  $i$ , approximating it as a first order GMRP distribution of time constant  $T_c$ , independent samples can be found every  $2 \cdot T_c$ , and the mean estimate  $\bar{x}_i$  for such data set is defined as:

$$\bar{x}_i = \frac{1}{N_i} \sum_{k=1}^{N_i} x_{i,k} \quad (5)$$

where:

$N_i$  is the number of independent samples in stationary data set  $x_i$   
 $x_{i,k}$  is the  $k^{th}$  independent sample in stationary data set  $x_i$

Similarly, the error on the mean estimate  $\bar{x}_i$  is defined as [22]:

$$\sigma_{\bar{x}_i}^2 = \frac{\sigma_{x_i}^2}{N_i} \quad (6)$$

where:

$N_i$  is the number of independent samples in stationary data set  $x_i$   
 $\sigma_{x_i}^2$  is the variance of stationary data set  $x_i$

Using a Weighted Least Squares estimator, an estimate of the orbit and clock error mean can be found with the expression:

$$\hat{x} = (H^T V^{-1} H)^{-1} H^T V^{-1} z \quad (7)$$

Substituting  $H, V$ , and  $z$  into Equation (7), we obtain:

$$\hat{x} = \frac{1}{\sum_i \sigma_{\bar{x}_i}^2} \sum_i \frac{\bar{x}_i}{\sigma_{\bar{x}_i}^2} \quad (8)$$

Using orbit and clock error data from 2018 and 2019, we obtain mean estimates of  $\hat{x}_{GPS} = 1.79$  cm and  $\hat{x}_{GAL} = 0.84$  cm. It is important to remember that the IGS reference files are provided with an accuracy of 2.5 cm. Therefore, the means obtained here are negligible.

These results are consistent with those obtained independently in [9], which also concluded that orbit and clock error of GPS and Galileo were zero mean over 1-year long durations. Therefore, in the following, we will model the orbit and clock errors as zero mean processes.

### Orbit and clock errors autocorrelation bounding

In prior work, we studied the impact of the moon and the sun on orbit and clock error time correlation. In this work, we will investigate the impact of satellite clock type. Figure 7 shows the normalized ACFs of GPS (left) and Galileo (right) orbit and clock errors for each clock type. In the left-hand-side charts of Figure 7, the differences in GPS clock errors observed in the time series in Figure 3 are difficult to observe in the ACF curves. Note that GPS has only 2 Cesium clocks to work with against 29 Rubidium clocks. Hence, it is difficult to generalize the Cesium results based on only 2 satellite clocks. In the right hand-side charts of Figure 7, the Galileo ACF curves show little difference between the RAFS and the PHM orbit and clock errors, but their time correlation decays significantly faster than for GPS clocks.

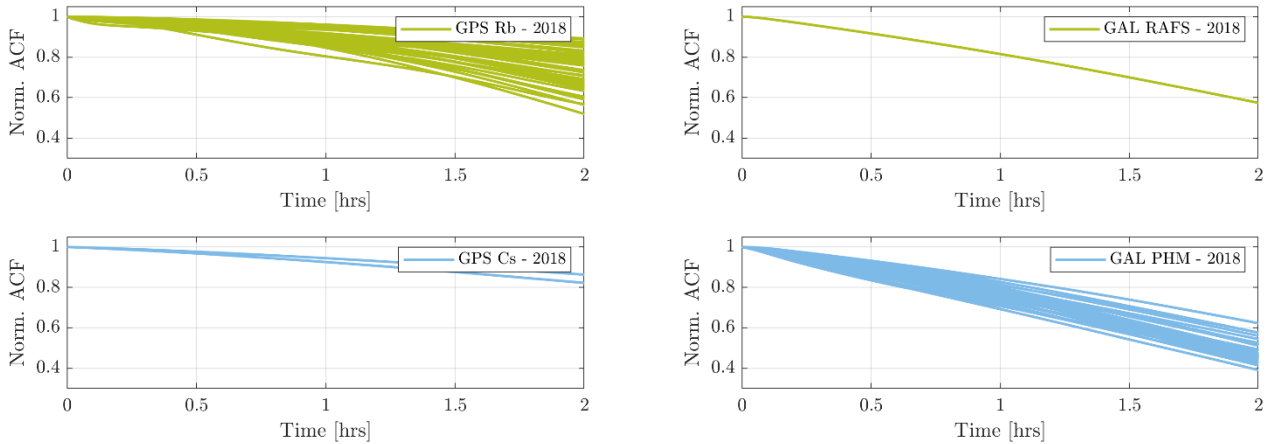


Figure 7: Impact of satellite clocks on GPS (left) and Galileo (right) orbit and clock error ACFs

For integrity evaluation, we could use a clock model that accounts for the worst satellite clock. Or, if we were able to identify a satellite’s clock type at the user receiver, then we could use separate, more accurate models for each clock. However, neither the LNAV nor CNAV GPS messages specify the satellite clock, which can change for a given PRN. Therefore, implementing separate clock-type-dependent models would require changes in the current ARAIM Integrity Support Message (ISM) structure, or new assumptions on a receiver’s access to Notice Advisory to Navstar Users (NANUs). For simplicity’s sake, we will bound all satellites together instead of differentiating by clocks (or even blocks).

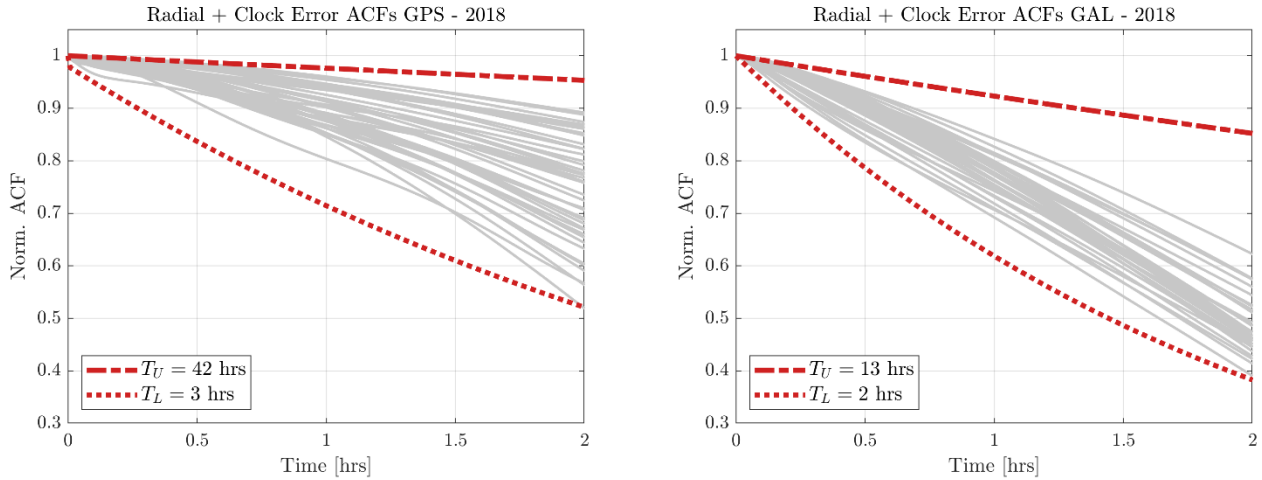


Figure 8: ACF bounding for GPS (left) and Galileo (right) satellites

Figure 8 shows ACFs of the radial-plus-clock error of each GPS (left) and Galileo (right) satellites, with data taken over stationary periods of 2018. GPS satellites are lower-bounded and upper-bounded using GMRPs with time constants of 3 hours and 42 hours, respectively. Galileo satellites are bounded with GMRPs with time constants of 2 hours and 13 hours.

This approach to bound the orbit and clock errors over time has the advantage of being easy to visualize and to understand. However, the bounds obtained here are quite loose and will ultimately lead to very conservative results. Moreover, note that we have here limited the lag times to 2 hours. If we want to extend the bounding process to larger durations (e.g. to the longest flight duration is about 18 hours), the ACF curves start to oscillate and even reach negative values that cannot be lower-bounded using first order GMRPs (as observed and tackled in [23]). The following section approaches modeling by bounding the PSD, which presents the advantage of being less restrictive, and more intuitive than autocorrelation bounding.

## Orbit and clock errors Power Spectral Density bounding

When it comes to estimating power spectral densities of stationary data, several methods exist [22], the most straightforward being the Discrete Fourier Transform (DFT) of the ACF. Reference [13] conjectures that error ACF values at time lags exceeding the duration of the Kalman filter's operation are not relevant and can, therefore, be set to any value (zero, for example). This conjecture is strictly true only for zero mean processes, but as we showed earlier a zero-mean assertion is justified in this application. To estimate the orbit and clock error PSDs, we used data collected over the entire year of 2018, and broken up into stationary segments. We then applied the PSD estimation algorithm used in [13] and summarized in Figure 9.

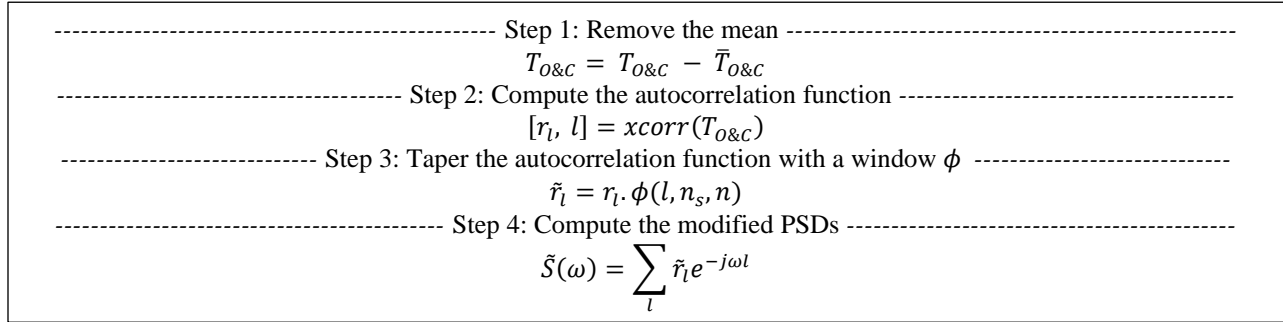


Figure 9: PSD estimation algorithm [13]

This algorithm uses a tapering window (see Figure 10) applied to the orbit and clock errors ACFs prior to the DFT to control spectral leakage. The figure on the left represents the window itself with respect to lag number. The figure on the right represents an example ACF with (black) and without (grey) tapering by the window. The sharp changes involved in simpler rectangular windows generate spectral leakage that diminishes the quality of the estimated PSD. The tapering window  $\phi$  function defined in [13] and used in this work smooths out the edges of the original rectangular window to reduce spectral leakage. This tapering window depends on two limit lag-time parameters:  $n_s$  and  $n$ .  $n$  is the maximum lag-time for which ACF values remain unchanged. ACF values associated to lags larger than  $n_s$  are set to zero. The farther apart  $n$  and  $n_s$  are from each other, the less spectral leakage is observed in the estimated PSD. In our case, because the longest satellite pass lasts 7 h, we choose 7 and 14 hours for  $n$  and  $n_s$ , respectively.

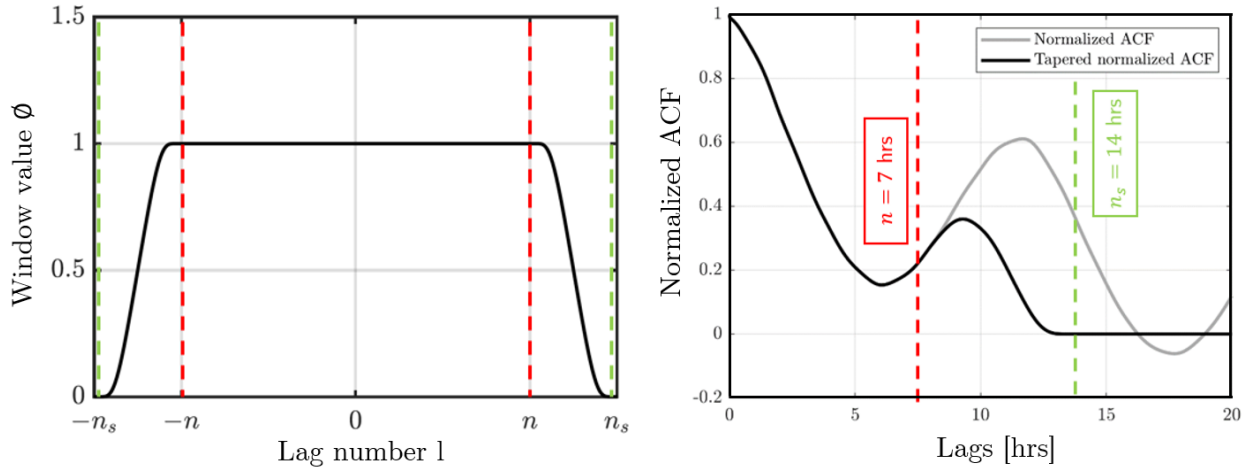


Figure 10: Tapering Window and its impact on an ACF [13]

The left plot in Figure 11 shows the estimated PSD curves for the GPS satellites. The blue curves represent the Cs satellites' orbit and clock errors and the green curves represent the Rb ones. The two types of clocks can again be differentiated, with the Cs curves mostly above the Rb ones. The Rb clock curves are lower, which means that the standard deviation of the errors is also lower, which matches previous observations.

Similarly, the right-hand-side plot in Figure 11 represents the Galileo orbit and clock error PSDs color-coded by clock type. Consistent with the time series and ACF observations, Galileo's orbit and clock errors from RAFS and PHM perform very

similarly based on the limited number of clock samples available. In both cases, bounding the two clock types separately would hardly improve the quality of the bound.

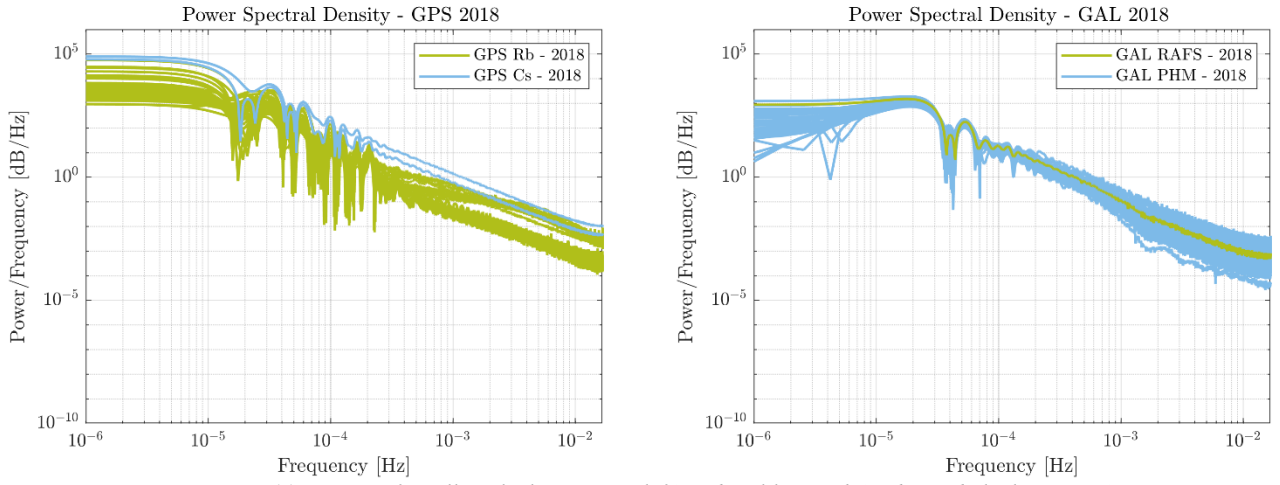


Figure 11: Impact of satellite clocks on GPS (left) and Galileo (right) orbit and clock error PSDs

Additionally, we note that resonant peaks can be observed in the PSDs of both constellations. The first GPS peak is located at a frequency of  $2.92 \times 10^{-5}$  Hz, which corresponds to a period of approximately 9.5 hours. The Galileo peak is located at approximately  $2.15 \times 10^{-5}$  Hz corresponding to 12.9 hours. GPS satellites have an orbit period of one half a sidereal day (23h 56m 4s) and will therefore take about 11.9 hours to orbit the earth. Galileo satellites on the other hand, will take about 14 hours to orbit the Earth. These values are close to the first peaks observed on the orbit and clock error's PSDs. It is interesting to note that if we take larger values for  $n_s$ , the ACFs at lags near the orbit period will be less attenuated, and therefore, the peaks observed on the PSDs tend to move closer to the orbit period.

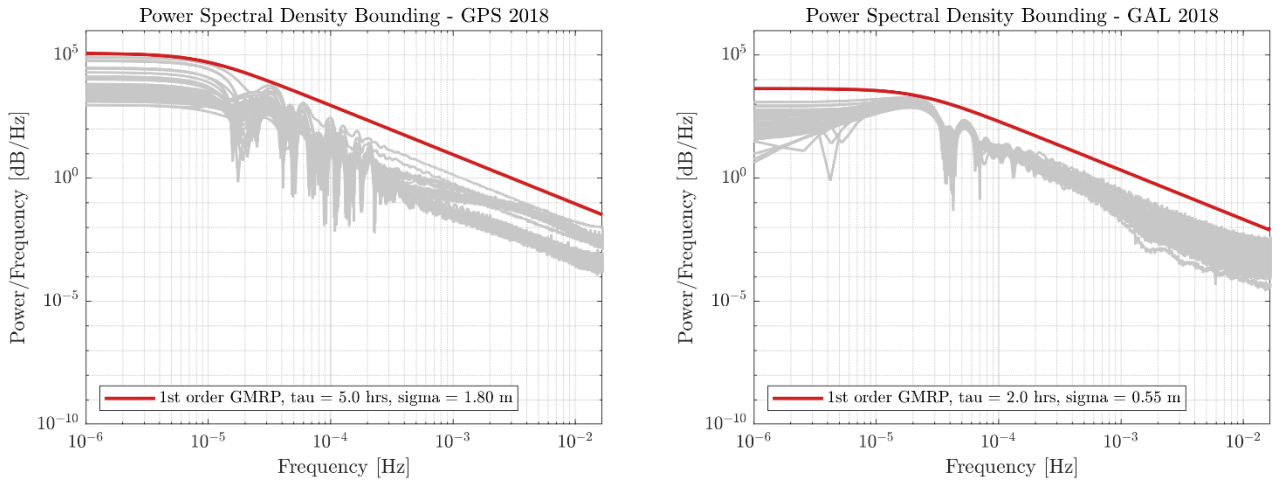


Figure 12: PSD bounding for GPS (left) and Galileo (right) satellites

To model the dynamics of orbit and clock errors over time, we gathered the orbit and clock errors of each satellite for each stationary dataset of 2018 and separated them by constellation. For each constellation, PSDs were upper-bounded by a first-order GMRP curve of time constant  $\tau$  and standard deviation  $\sigma_{Const}$ , using the expression [24]:

$$S(f) = (2\sigma_{Const}^2/\tau)/(1/\tau^2 + 4\pi^2 f^2) \quad (10)$$

Figure 12 shows the result. For the GPS constellation, the PSDs of orbit and clock errors were bounded using time constant  $\tau = 5$  hours and  $\sigma_{GPS} = 1.8$  meters. Similarly, the Galileo errors were bounded with  $\tau = 2$  hours and  $\sigma_{GAL} = 0.55$  meters.

Comparing these results with the previous modeling approach (see “autocorrelation bounding” section), we see that both constellation’s time constants are close to the lower bound, but always contained between the upper and lower bounds. GPS’s autocorrelation functions were upper and lower bounded with first-order GMRP of time constant 42 and 3 hours, and the PSD bounding approach results in a time constant of 5 hours. Galileo’s were upper and lower bounded with 13 and 2 hours, and the PSD bounding approach results in a time constant of 2 hours. This shows that both modeling approaches do not contradict each other.

### State Space model of Orbit and Clock errors

Let us assume we are trying to account for orbit and clock error in a nominal KF with model defined by its states  $F$ ,  $G$ , and  $H$ . Since the error we are trying to model is colored noise, its implementation in a KF will require state augmentation. Given that KF (with state vector  $x$ ), the state augmentation required to model orbit and clock errors is expressed in Equations (11) and (12) as:

$$\begin{bmatrix} x \\ x_a \end{bmatrix}_{k+1} = \begin{bmatrix} F & 0 \\ 0 & e^{-\Delta t/\tau} \end{bmatrix} \begin{bmatrix} x \\ x_a \end{bmatrix}_k + \begin{bmatrix} G & 0 \\ 0 & I \end{bmatrix} \begin{bmatrix} \omega \\ \omega_a \end{bmatrix}_k \quad (11)$$

$$z = \begin{bmatrix} H & I \end{bmatrix} \begin{bmatrix} x \\ x_a \end{bmatrix} + v_\omega \quad (12)$$

where:

$\Delta t$  is the sampling rate (in seconds)

$\omega_a$  is the augmented process noise which is normally distributed with zero mean and variance  $(1 - e^{-\frac{2\Delta t}{\tau}})\sigma_{const}^2$

$x_a$  is the augmented state (i.e. first order GRMP model of orbit and clock errors), with  $x_a(0) \sim \mathcal{N}(0, \sigma_{const}^2)$

### CONCLUSION

In this paper, we developed new stochastic GNSS orbit and clock error models. These models are useful for time-sequential navigation systems including Global Navigation Satellite Systems (GNSS) integrated with inertial navigation systems (INS) or dual-frequency, multi-constellation, sequential Advanced Receiver Autonomous Integrity Monitoring (ARAIM).

Stationarity analysis were performed on empirical orbit and clock error data using two statistical tests: one on the variance of the errors, and another one on their distribution, hence ensuring both main characteristics of a stationary process were met.

To bound orbit and clock errors, two approaches were investigated. A time-domain approach used first order GMRP models to upper and lower bound the error’s ACFs. This model was deemed to be extremely conservative. A frequency-domain analysis, in which the PSDs were upper-bounded using a first order GMRP, was chosen instead. In both domains, the GPS satellite clocks were showed to drive the behavior of the errors. This was not the case for the Galileo clocks. Because the current ARAIM ISM does not differentiate the URAs according to clock type, we decided to bound all satellites using only two models, one for each constellation.

### ACKNOWLEDGMENTS

The authors would like to thank the Federal Aviation Administration (FAA) for their support of this research. However, the opinions in this paper are our own and do not necessarily represent those of any other person or organization.

### REFERENCES

- [1] C. Tanil, S. Khanafseh, M. Joerger und B. Pervan, “An INS Monitor to Detect GNSS Spoofers Capable of Tracking Vehicle Position,” *IEEE Transactions on Aerospace and Electronics*, Bd. 64.1, pp. 131-143, 2018.
- [2] Working Group C, “ARAIM Technical Subgroup. Interim Report Issue 1.0.,” EU-US Cooperation on Satellite Navigation, 2012.

- [3] Working Group C, "ARAIM Technical Subgroup. Milestone 2.0 Report," EU-US Cooperation on Satellite Navigation, 2014.
- [4] Working Group C, "ARAIM Technical Subgroup. Milestone 3.0 Report," EU-US Cooperation on Satellite Navigation, 2016.
- [5] M. Joerger und B. Pervan, "Multi-Constellation ARAIM Exploiting Satellite Motion," *NAVIGATION, Journal of the Institute of Navigation*, Bd. 67, Nr. 2, pp. 235-253, 2020.
- [6] S. Langel, "Bounding Estimation Integrity Risk for Linear Systems With Structure Stochastic Modeling Uncertainty," PhD Dissertation, May 2014.
- [7] S. Langel, O. Garcia-Crespillo und M. Joerger, "Bounding Sequential Estimation Errors Due to Gauss-Markov Noise with Uncertain Time Constants," in *Proceedings of the 32nd International Technical Meeting of The Satellite Division of the Institute of Navigation (ION GNSS+ 2019)*, Miami, FL, 2019.
- [8] E. Gallon, M. Joerger, S. Perea und B. Pervan, "Error model development for ARAIM exploiting satellite motion," in *Proceedings of ION GNSS+*, Miami, FL, 2019.
- [9] S. D. Perea, "Design of an Integrity Support Message for Offline Advanced RAIM," PhD Dissertation, May 2019.
- [10] B. DeCleene, "Defining Pseudorange Integrity Overbounding," in *Proc. ION GPS 2000*, Salt Lake City, UT, 2000.
- [11] J. Rife, S. Pullen, P. Enge und B. Pervan, "Paired Overbounding for Nonideal LAAS and WAAS Error Distributions," *IEEE TAES*, Bd. 42, Nr. 4, pp. 1386-1395, 2006.
- [12] E. Gallon, M. Joerger und B. Pervan, "Robust Modeling of Tropospheric Delay Dynamics for Sequential Positioning," in *Proceedings of IEEE/ION PLANS 2020*, Portland, 2020.
- [13] S. Langel, O. Garcia-Crespillo und M. Joerger, "A New Approach for Modeling Correlated Gaussian Errors Using Frequency Domain," in *IEEE/ION PLANS 2020*, Portland, OR, 2020.
- [14] International GNSS Service, "Data Repository," [Online]. Available: <ftp://cddis.gsfc.nasa.gov/gps/data/>.
- [15] M. Schenewerk, "A Brief Review of basic GPS Orbit Interpolation Strategies," *GPS Solutions*, Bd. 6, Nr. 4, pp. 265-267, March 2003.
- [16] Stanford University, "GPS Ephemeris Repository," [Online]. Available: <https://gps.stanford.edu/suglephemeris-files>.
- [17] Centre National d'Etudes Spatiales, "Broadcast ephemeris data repository," [Online]. Available: <ftp://serenad-public.cnes.fr/SERENAD0/FROM NTMFV2/NAV/>.
- [18] International GNSS Service, "Antex files," [Online]. Available: [ftp://ftp.igs.org/pub/station/general/pcv\\_archive/](ftp://ftp.igs.org/pub/station/general/pcv_archive/).
- [19] P. J. Teunissen und O. Montenbruck, *Springer Handbook of Global Navigation Satellite Systems*, Springer International Publishing AG 2017, 2017.
- [20] H. Levene, "Robust tests for equality of variances," *Ingram Olkin; Harold Hotelling; et al. (eds). Contributions to Probability and Statistics: Essays in Honor of Harold Hotelling. Stanford University Press.*, pp. 278 - 292, 1960.
- [21] F. Massey, "The Kolmogorov-Smirnov Test for Goodness of Fit," *Journal of the American Statistical Association*, Bd. 46, Nr. 253, pp. 68 - 78, 1951.
- [22] J. S. Bendat und A. G. Piersol, *Random Data Analysis and Measurement Procedures*, New Jersey: John Wiley & Sons, 2010.
- [23] S. K. Jada und M. Joerger, "GMP-Overbound Parameter Determination for Measurement Error Time Correlation Modeling," in *International Technical Meeting (ITM)*, San Diego, California, 2020.
- [24] C. Chatfield, *The Analysis of Time Series: An Introduction*, Sixth Edition, CRC Press, 2016.
- [25] RTCA, "Minimum Operational Performance Standards for Global Positioning System/Wide Area Augmentation System Airborne Equipment system, RTCA DO-229E," 2016.